Structural and chemical characterization of Douglas-fir and red alder biochar

Samuel Olajide
Department of Wood Science and Engineering, Oregon State University, Corvallis, OR 97331, USA Email: samuel.olajide@oregonstate.edu

Tomiwa Haruna
Department of Wood Science and Engineering, Oregon State University, Corvallis, OR 97331, USA Email: harunatomijeje2000@gmail.com

Alhassan Ibrahim
Department of Wood Science and Engineering, Oregon State University, Corvallis, OR 97331, USA Email: hassanbinrazak157@yahoo.com

Robert J. Macias
Department of Wood Science and Engineering, Oregon State University, Corvallis, OR 97331, USA Email: maciasnr@oregonstate.edu

Gerald Presley†
Department of Wood Science and Engineering, Oregon State University, Corvallis, OR 97331, USA Email: gerald.presley@oregonstate.edu

*Islam Hafez**
Department of Wood Science and Engineering, Oregon State University, Corvallis, OR 97331, USA Email: islam.hafez@oregonstate.edu

(Received 23 July 2026)

Abstract: Biochar properties are often interpreted primarily as a function of pyrolysis temperature, but feedstock compositional differences can also influence the structural evolution of woody biochar. This study provides a complementary characterization of biochar produced from Douglas-fir (*Pseudotsuga menziesii*) softwood and red alder (*Alnus rubra*) hardwood forest residues under comparable pyrolysis conditions. Douglas-fir biochar was produced at 350°C, 500°C, and 700°C, while red alder biochar was produced at 500°C, using fast pyrolysis in a custom-built fluidized bed reactor. The biochar was characterized using proximate and elemental analysis, CO_2 BET surface area, pH, Raman spectroscopy, Fourier transform infrared spectroscopy, and thermogravimetric analysis. Within the Douglas-fir series, increasing pyrolysis temperature decreased biochar yield, volatile matter, and oxygenated functional groups, while increasing gas yield, fixed carbon, alkalinity, surface area, and thermal stability. Under identical pyrolysis conditions at 500°C, red alder biochar retained greater C-H and O-H functionality and higher O/C and H/C ratios than Douglas-fir biochar. These differences were consistent with feedstock compositional differences, particularly the higher hemicellulose content and syringyl-guaiacyl lignin composition of red alder, which may favor retention of hydrogenated and oxygenated structures. In contrast, the higher guaiacyl lignin content of Douglas-fir may have contributed to greater carbon condensation, deoxygenation, and aromatization. Raman analysis showed increasing I_D/I_G ratio with pyrolysis temperature, indicating changes in carbon structure during thermal reorganization. Feedstock differences were evaluated at 500°C, while temperature effects were assessed only for Douglas-fir. The results from this study link feedstock composition with differences in functional-group retention, carbon condensation, and thermal stability.

Keywords: Biochar; Pyrolysis temperature; Biomass feedstock; Characterization; Thermal stability; Functional groups.

Introduction

Biochar is a carbon-rich, porous by-product of biomass pyrolysis under oxygen-limited conditions (Manyà 2012; Kamarudin et al. 2022). It is widely used as a multifunctional material in soil fertilization, metal immobilization, water treatment, and construction applications (Chen et al. 2011; Awad et al. 2012; Bolan et al. 2022). Its utility arises from tunable properties, including high porosity, large surface area, variable surface chemistry, and chemical stability (Liu et al. 2015; Hassan et al. 2020). As a soil amendment, biochar improves productivity by increasing soil organic matter, water retention, microbial activity, and nutrient retention (Glaser et al. 2002; Sopeña et al. 2012; Bian et al. 2013; Sun et al. 2017; Yaashikaa et al.

* Corresponding author
† Society of Wood Science & Technology member

2020). Its sorption properties also enable removal of pollutants, including toxic heavy metals, from water (Ahmad et al. 2014; Shakoor et al. 2020). In construction, biochar has been incorporated into concrete and cement composites to improve thermal insulation, chemical stability, and flammability resistance (Gupta et al. 2018; Restuccia et al. 2020; Legan et al. 2022), and into polymer composites to enhance mechanical strength and thermal resistance (Das et al. 2015; Zhang et al. 2022).

Despite its broad applicability, biochar properties are highly variable and are strongly influenced by biomass feedstock and pyrolysis conditions (Ahmad et al. 2012; Zhao et al. 2013). Feedstock type influences the chemical composition, structural features, and functional potential of the resulting biochar (Gaskin et al. 2008; Yuan et al. 2011). Common feedstocks include animal waste, industrial waste, sewage sludge, wood chips, food waste, agricultural residues, and forest residues (Bedia et al. 2018). Leng et al. (2021) classified biochar feedstocks as wood and woody biomass, herbaceous and agricultural biomass, manure/waste biomass, and algae biomass. Lignocellulosic feedstocks differ in cellulose, hemicellulose, lignin, extractives, and inorganic contents, which influence biochar yield, elemental composition, and carbon stability (Tomczyk et al. 2020; Chaturvedi et al. 2023).

Biochar characteristics are also shaped by reactor design and production conditions, particularly pyrolysis temperature (Sun et al. 2014; Ahmad et al. 2014; Manyà et al. 2018). Higher temperatures generally reduce biochar yield through increased organic matter volatilization and secondary cracking, while promoting CO_2/CH_4 evolution, carbon densification, and formation of more aromatic, carbon-rich structures (Novak et al. 2009; Sun et al. 2012). Elemental composition typically shifts toward higher carbon content and aromaticity, with lower hydrogen and oxygen contents, producing a less polar and more hydrophobic material (Ahmad et al. 2014). The effects of feedstock and pyrolysis temperature are complex and may act independently or interactively (Tripathi et al. 2016; Ippolito et al. 2020; Tomczyk et al. 2020). For example, the temperature that maximizes surface area can vary with feedstock properties (Sharma et al. 2015; Kan et al. 2016).

Although the effects of feedstock type and pyrolysis temperature on biochar properties have been widely studied, direct comparative studies of Douglas-fir and red alder forest-residue biochar produced under comparable pyrolysis conditions appear to be limited. This species-specific comparison is relevant because Douglas-fir and red alder are two important softwood and hardwood resources in the US with different lignocellulosic composition, ash content, extractives, and lignin chemistry. These differences may influence the extent of functional-group retention, deoxygenation, mineral-associated residue formation, aromatization, and carbon condensation during pyrolysis. Therefore, this study provides a complementary characterization of Douglas-fir biochar across different pyrolysis temperatures and of Douglas-fir and red alder biochar produced at 500°C. The 500°C comparison was used to explore potential relationships between feedstock composition of these two species and variation in surface functionality, elemental composition, thermal stability, and Raman spectral features.

Materials and methods

Douglas-fir (*Pseudotsuga menziesii)* softwood and red alder (*Alnus rubra)* hardwood, composed of mixed size branches, bark and bole wood, were used as raw materials for pyrolysis. These raw materials were sourced from multiple locations in Oregon.

Production of biochar

Wood particles were air-dried to 10% dry-basis moisture content (MC). The particles were ground using a 3 hp CF 198 model electric hammer mill (PelletMasters, WI, USA), and sieved through a 0.5 mm W.S Tyler Incorporated standard testing sieve before pyrolysis. Biochar was produced in a custom-built fluidized bed pyrolyzer previously described in detail by Macias et al. (2026). The reactor core consisted of a 304 stainless-steel, Schedule 40 tube approximately 54 in. (1.37 m) in length and 3 in. (7.62 cm) in nominal diameter. The reactor was heated externally by two independently controlled furnace sections equipped with four Watlow electric heating elements (2 × 1.8 kW and 2 × 2.5 kW; 8.6 kW total installed power) and PID temperature controllers. Internal thermocouples positioned along the reactor were used to continuously monitor reactor temperature. No silica sand or other inert bed material was used in these experiments because the recovered biochar was intended for subsequent physicochemical characterization. Fluidization was therefore achieved directly with the biomass and char particles present in the reactor, avoiding contamination or dilution of the recovered biochar with an external mineral bed material. High-purity nitrogen was introduced through the bottom plenum and gas-distribution screen and supplied using an Alicat mass-flow controller at approximately 4 SLPM. The standard volumetric flow rate was referenced to 25°C and approximately 1 atm. Based on the internal cross-sectional area (3-in.) of the reactor, there was a correction of the gas volumetric flow for reactor temperature. The corresponding superficial nitrogen velocities were approximately 0.029, 0.036, and 0.046 m s^{-1} at 350°C,

500C°, and 700°C, respectively. For the 0.5-mm biomass particles, the minimum fluidization velocity was estimated using the Kunii and Levenspiel fluidization correlations and was on the order of 0.01 m s^{-1}, depending on feedstock properties and operating temperature (Kunii and Levenspiel 1997). The selected nitrogen flow therefore maintained the solids above the estimated minimum fluidization condition throughout the experiments.

Before biomass feeding, the desired pyrolysis temperature was entered into the PID controllers and the reactor was heated under continuous nitrogen flow. Once the internal thermocouples reached the prescribed target temperature, the reactor was maintained at that temperature for an additional 2 h to ensure thermal equilibrium and a stable temperature profile throughout the reactor. Biomass feeding was initiated only after this stabilization period. The same procedure was followed for all pyrolysis temperatures investigated.

Approximately 2 kg of each biomass was subsequently fed into the reactor at 40 g/min, corresponding to a feeding period of approximately 50 min, while the reactor was maintained at the prescribed pyrolysis temperature. Following completion of biomass feeding, the reactor was maintained at the target temperature for an additional 30 min to allow further devolatilization of residual material. Douglas-fir biochar produced at 350°C, 500°C, and 700°C was referred to as DF 350, DF 500, and DF 700, respectively, whereas red alder biochar produced at 500°C was referred to as RA 500. Three independent pyrolysis runs were conducted for each condition.

After pyrolysis, the electric heaters were switched off while nitrogen flow was continuously maintained during cooling. The biochar therefore remained under an inert atmosphere until the reactor approached room temperature, minimizing oxidation of the freshly produced char prior to collection and storage.

Biochar and biomass characterization

Proximate analysis, BET surface area analysis, and pH measurement

Moisture content, volatile matter (VM), and ash content (AC) were determined using Equations (1-3) and a modified ASTM D1762-84 Standard Test Method for Chemical Analysis of Wood Charcoal (ASTM International 2021) adapted for biochar analysis in a muffle furnace (Aldayyat et al. 2021; Chisté et al. 2024). Crucibles were pre-fired at 750°C for 6 h and cooled to 105°C to volatilize residual organic substances before analysis. MC was determined by oven-drying samples at 105°C for 48 h. VM was measured by heating oven-dried samples in lidded crucibles in a preheated muffle furnace at 950°C for approximately 7 min, followed by cooling in a desiccator and recording weight loss. AC was determined from the residue remaining after combusting oven-dried samples in open crucibles at 750°C for 6 h.

$$MC\ (\%) = \frac{Wet\ weight - Dry\ weight\ at\ 105\ °C}{Dry\ weight\ at\ 105\ °C}\ x\ 100 \quad [1]$$

$$VM\ (\%) = \frac{Dry\ weight\ at\ 105\ °C - Dry\ weight\ at\ 950\ °C}{Dry\ weight\ at\ 105\ °C}\ x\ 100 \quad [2]$$

$$AC\ (\%) = \frac{Wet\ weight - Dry\ weight\ at\ 750\ °C}{Dry\ weight\ at\ 105\ °C}\ x\ 100 \quad [3]$$

Fixed carbon (FC) and biochar yield (Y) were calculated according to equations (4) and (5), respectively. All values were expressed on a dry weight basis.

$$FC\ (\%) = 100 - (MC + VM + AC) \quad [4]$$

$$Y\ (\%) = \frac{Biochar\ mass}{Dry\ weight\ of\ biomass\ at\ 105\ °C}\ x\ 100 \quad [5]$$

Carbon dioxide adsorption isotherms were measured at 273 K using a Micromeritics TriStar II PLUS Surface Area and Porosity Analyzer (Norcross, GA, USA). Before analysis, samples were degassed for 18 h at 453 K under vacuum using a Micromeritics VacPrep 061 Degassing System. CO_2 adsorption isotherms were collected over $p/p_0 = 10^{-5} - 0.03$ using 75 equilibration points to capture low-pressure adsorption associated with microporosity. Apparent CO_2 BET surface area was calculated from the adsorption isotherms (Dubinin and Radushkevich 1947; Dubinin et al. 1947).

Biochar pH was measured following Singh et al. (2017). Approximately 5 g of biochar was dispersed in 50 mL distilled water and shaken for 1 h at room temperature using an ONiLAB orbital shaker (Walnut, CA) at 150 rpm. The suspension was allowed to equilibrate for 30 min before pH measurement with an OHAUS Starter 2200 bench pH meter (Parsippany, NJ).

Biomass characterization

The detailed biomass characterization of the material used in this study has been previously reported by Macias et al. (2026). Cellulose, hemicellulose, lignin, ash, and extractives contents were determined according to the standard compositional analysis procedures (Sluiter et al. 2012). Briefly, extractives were removed prior to analysis, and the remaining structural

biomass was fractionated to quantify cellulose, hemicellulose, and lignin contents. Lignin was determined as the sum of acid-insoluble and acid-soluble fractions, while ash was measured gravimetrically after combustion. All compositional values were expressed on an oven-dry weight basis.

Raman and Fourier transform infrared spectroscopy

Raman spectra were collected using a Shimadzu Airsight Raman Microscope (Columbia, MD) to assess carbon structure. Spectra were acquired with a 532 nm laser and 50× objective over 500-4000 cm^{-1}, averaging 80 scans. All spectra were baseline corrected. Fourier transform infrared spectroscopy (FT-IR) spectra were collected using a Shimadzu IRTracer-100 (Columbia, MD) to identify functional groups. Spectra were acquired in absorbance mode at 4 cm^{-1} resolution from 500 to 4000 cm^{-1}, averaging 45 scans. All FT-IR spectra were baseline corrected and normalized to the maximum absorbance peak to enable comparison among samples.

Elemental analysis

The relative carbon, hydrogen, nitrogen, and oxygen contents of biochar were determined using a LECO CHN828 series analyzer (St. Joseph, MI). Approximately 75 mg of biochar was used per run, consistent with the instrument calibration range of 70–140 mg. Oxygen content was calculated by difference after measuring carbon, hydrogen, and nitrogen.

Thermogravimetric analysis

Thermogravimetric analysis (TGA) was performed using a TA Instrument thermogravimetry analyzer (New Castle, DE), TGA 550, to assess the biochar's thermal stability and degradation profile. Approximately 7 to 10 mg of biochar was heated from room temperature to 800°C at a 10°C/min heating rate, under a nitrogen atmosphere.

Scanning electron microscopy

The morphology of the samples was observed through scanning electron microscopy (SEM) (FEI Quanta 600 FEG) with a high voltage of 3.0 kV and a working distance ranging from 9.8 mm to 10 mm. The SEM images were obtained from Douglas-fir and red alder biochar produced in a separate slow pyrolysis experiment and were not collected from the fast-pyrolysis biochar used for the other characterization analyses in this study. Samples were sputter-coated with gold before imaging, and images were acquired at magnifications ranging from 250x to 2500x.

Statistical analysis

A two-sample t-test was used to compare two independent groups, and one-way ANOVA was used to compare means among more than two independent groups. Tukey's honest significant difference test was used for post hoc pairwise comparisons. All analyses were performed in R at a 95% confidence level.

Results and discussion

Proximate analysis, BET surface area analysis, and pH measurement

The three pyrolysis product yields are shown in Figure 1. Biochar, bio-oil, and gas yields varied with pyrolysis temperature and feedstock. Biochar yield decreased with increasing temperature (Figure 1b), consistent with trends reported for apa wood, iroko wood, and palm kernel shell by Titiladunayo et al. (2012). DF 350 produced the highest biochar yield (34%), whereas DF 500 and DF 700 each produced approximately 18%. This reduction is consistent with increased thermal cracking and decomposition of lignocellulosic components at higher temperatures (Cárdenas-Aguiar et al. 2017). RA 500 produced a slightly higher biochar yield (21%) than DF 500 (18%), showing a relatively small difference in biochar yield between the two feedstocks.

Similar to biochar yield, DF 500 and RA 500 showed similar bio-oil yield at 500°C, producing 56% and 58%, respectively. Tang et al. (2020) similarly reported a 60% bio-oil yield from a machine-learning analysis of 264 bio-oil yield datasets, influenced by feedstock composition. In contrast, pyrolysis temperature strongly affected DF bio-oil yield. DF 500 produced the highest bio-oil yield (56%), compared with 45% for DF 350 which is consistent with lower degree of devolatilization at the lower temperature. Bio-oil yield declined further to 38% for DF 700, indicating additional devolatilization and greater gas formation. Accordingly, DF 700 had the highest gas yield (44%), whereas DF 350 and DF 500 produced 22% and 25%, respectively, consistent with trends reported by Chhiti et al. (2012) and He et al. (2009). RA 500 produced 21% gas, compared with 25% for DF 500. suggesting that feedstock composition may reduce gas formation. Proximate analysis was therefore conducted to further evaluate the effects of feedstock and pyrolysis temperature.

Proximate analysis provides the compositional breakdown of biochar into MC, VM, AC, and FC. Table 1 presents the proximate composition of the four biochar samples. Two-sample t-tests showed significant differences in VM ($p = 0.003$) and FC ($p = 0.0074$) between DF 500 and RA 500. One-way ANOVA showed no significant difference in MC among the DF biochar ($p = 0.3328$), but significant differences in VM ($p = 0.0016$), AC ($p = 0.0002$), and FC ($p = 0.0041$) among DF 350, DF 500, and DF 700.

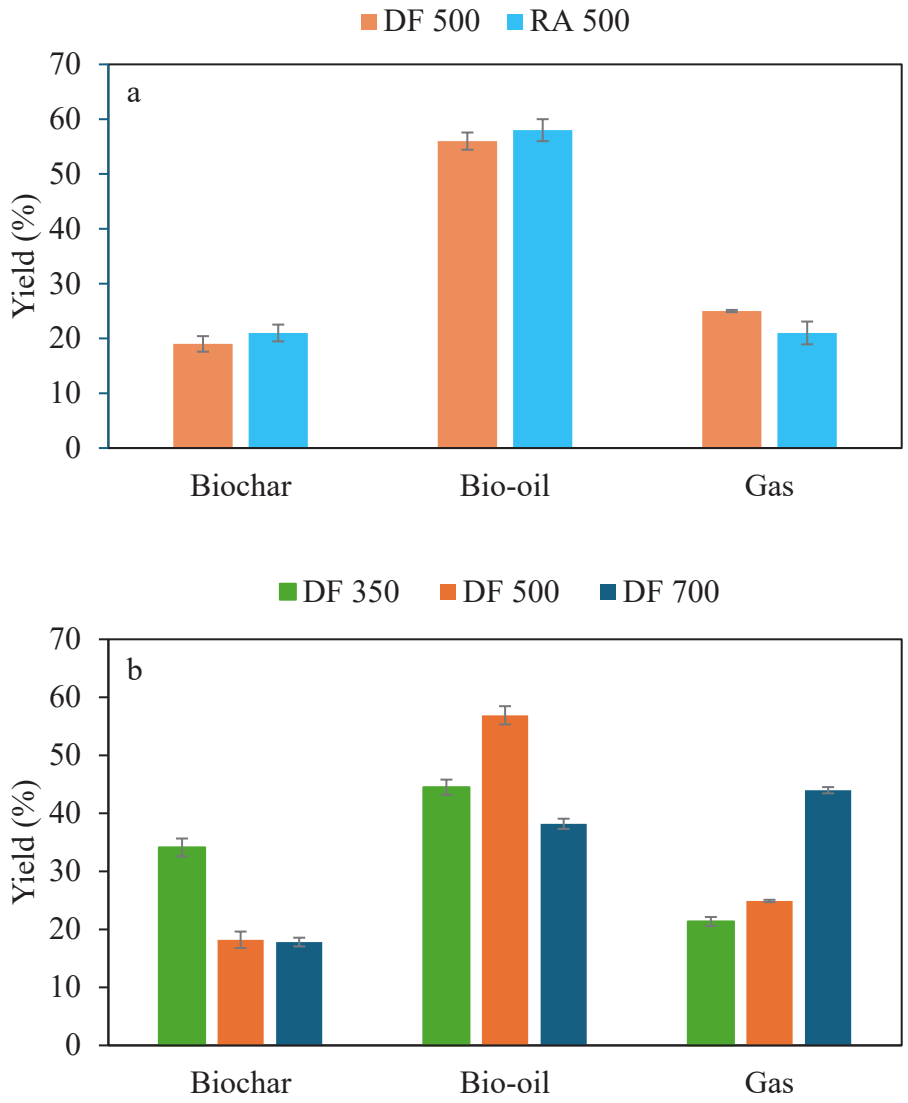


Figure 1. Mean and one standard deviation of (a) biomass feedstock effects on pyrolysis product yields on DF 500 and RA 500; and (b) temperature effects on pyrolysis product yields on DF 350, DF 500, and DF 700.

Table 1. Biochar properties as influenced by biomass feedstock and pyrolysis temperatures.

Sample	Proximate analysis (%) *			
	MC	VM	AC	FC
DF 350	3.06 ± 1.05 ^{a}	37.35 ± 7.85 ^{a}	2.03 ± 0.02 ^{a}	57.56 ± 8.84 ^{a}
DF 500	3.77 ± 0.61 ^{a}	14.04 ± 1.51 ^{b}	10.95 ± 2.07 ^{b}	71.24 ± 2.54 ^{bc}
DF 700	3.07 ± 1.05 ^{a}	11.54 ± 4.12 ^{b}	2.38 ± 0.61 ^{a}	83.01 ± 2.78 ^{c}
RA 500	2.37 ± 0.60	22.03 ± 1.54	11.86 ± 0.56	63.73 ± 0.52

* mean ± one standard deviation of three replicates. One-way ANOVA followed by Tukey's post hoc test was performed separately for each property using DF 350, DF 500, and DF 700. Within each column, means sharing at least one letter are not significantly different ($\alpha = 0.05$); letters are assigned independently for each column. Separate t-test comparisons between DF 500 and RA 500 are reported in the Results and discussion.

All biochar samples had low MC values (2.37%–3.77%), typical of biochar (Das et al. 2015). The lower MC of RA 500 (2.37%) compared with DF 500 (3.77%) may reflect feedstock-dependent pore structure differences. CO_2 BET analysis supported this interpretation where DF 500 had a higher equivalent surface area (337.53 $m^2\ g^{-1}$) than RA 500 (249.04 $m^2\ g^{-1}$), which may contribute to a greater moisture retention.

VM decreased significantly with increasing pyrolysis temperature in DF biochar, from 37.35% in DF 350 to 11.54% in DF 700. This trend is consistent with reports that higher temperatures promote devolatilization and removal of thermally unstable compounds (Ahmad et al. 2014; Suliman et al. 2016; Tomczyk et al. 2020). The sharp decrease from DF

350 to DF 500 (14.04%) indicates a transition from low-temperature biochar to a more condensed carbon structure. VM was also significantly higher in RA 500 (22.03%) than in DF 500 (14.04%), reflecting feedstock differences in composition and thermal degradation behavior; RA may contain more volatilization-prone components (Zhao et al. 2013).

AC varied among samples. DF 500 (10.95%) and RA 500 (11.86%) had the highest ash contents, with no significant difference between them by two-sample t-test ($p = 0.5017$). The higher AC in DF 500 than in DF 350 (2.03%) and DF 700 (2.38%) may indicate incomplete combustion or retention of thermally stable mineral matter.

Ash content decreased at 700°C, likely due to mineral volatilization (Mohan et al. 2014). In contrast, FC increased with pyrolysis temperature, consistent with previous studies (Demirbas 2007; Keiluweit et al. 2010). DF 700 had the highest FC (83.01%), indicating a highly carbonized and stable biochar, whereas DF 350 had the lowest FC (57.56%). Additionally, DF 500 and RA 500 showed substantial carbon retention, with FC values of 71.24% and 63.73%, respectively; however, RA 500 had a significantly lower mean FC than DF 500, again reflecting feedstock compositional differences. The inverse relationship between VM and FC confirms progressive carbon enrichment as volatiles are released during pyrolysis.

Biochar pH ranged from moderately alkaline at lower pyrolysis temperature to strongly alkaline at higher temperatures. DF 350 had an average pH of 8.04, reflecting partial retention of carboxylic acids, phenolic groups, and high residual VM, as indicated by proximate analysis (Domingues et al. 2017; Chisté et al. 2024). With the progressive loss of acidic functional groups and VM, pH increased significantly to 10.34 in DF 500 and remained slightly lower in DF 700 (10.11). RA 500 showed a similar pH to DF 500, averaging 10.20. These results indicate that pyrolysis temperature strongly influences surface chemistry by shifting the balance between acidic and basic functional groups, making it a key factor controlling biochar alkalinity. Higher-temperature biochar generally exhibited stronger alkaline reactions, consistent with previous studies (Silber et al. 2010; Yuan et al. 2011; Manyà 2012; Xu et al. 2012; Keshvardoostchokami et al. 2023).

Raman and FT-IR spectroscopy

Raman spectroscopy characterizes the structural evolution of carbon-based materials. Biochar and other carbonaceous materials exhibit several diagnostic Raman bands. The D band (~1350 cm^{-1}) is commonly associated with disordered carbon structures (Tagliaferro et al. 2020). The G band, typically near 1580 cm^{-1}, is associated with aromatic carbon structures (Datsyuk et al. 2008). The D/G intensity ratio (I_D/I_G) is commonly used to evaluate changes in biochar carbon structure. However, its relationship with structural ordering is not necessarily monotonic in disordered carbon materials. The 2D band, located near 2850 cm^{-1}, is a second-order overtone of the D band and can provide additional information on changes in carbon structures (Childres et al. 2013; De Sousa et al. 2020).

Figure 2a shows the Raman spectra of RA 500 and DF 500 highlighting the D, G, and 2D bands. RA 500 and DF 500 exhibited similar overall Raman features, although differences in peak intensity were observed under the measurement conditions. Figure 2b shows the Raman spectra of DF biochar produced at 350°C, 500°C, and 700°C; DF 700 showed lower Raman intensity than DF 350 and DF 500. These peak features indicate the presence of aromatic clusters in all samples (Fuertes et al. 2010). The I_D/I_G ratios are presented in Table 2. RA 500 and DF 500 had comparable I_D/I_G ratios of 0.70 and 0.68, respectively,

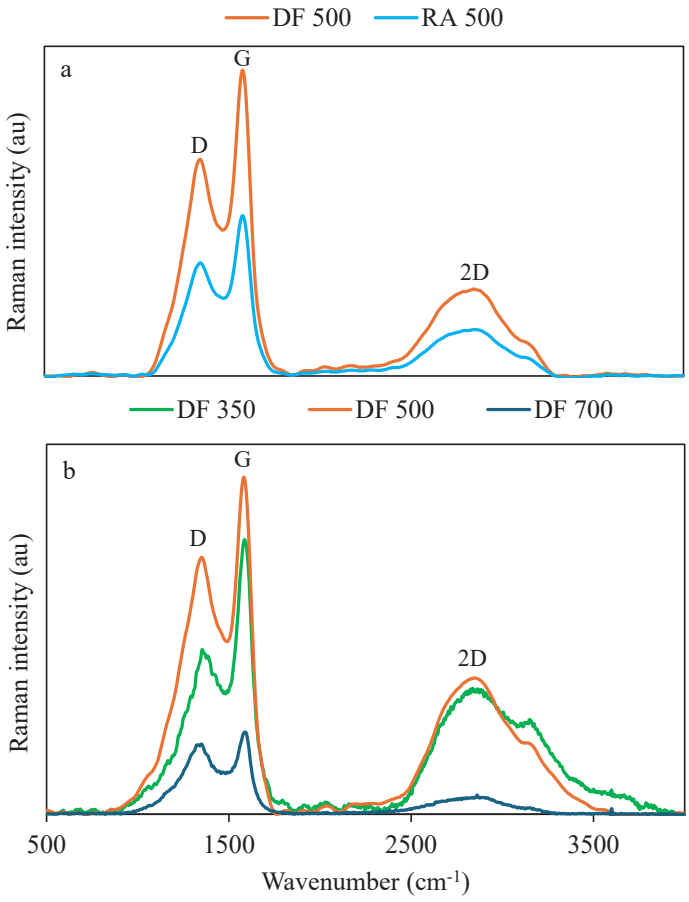


Figure 2. Raman spectra comparing the D, G, and 2D bands on (a) the effects of biomass feedstock on DF 500 and RA 500; and (b) temperature effects on DF 350, DF 500, and DF 700.

Table 2. I_D/I_G ratio results of biochar samples.

Sample	Pyrolysis temperature (°C)	I_D/I_G ratio *
RA 500	500	0.70 ± 0.04
DF 350	350	0.66 ± 0.05
DF 500	500	0.68 ± 0.04
DF 700	700	0.80 ± 0.03

* mean ± one standard deviation of three replicates.

showing similar Raman D/G characteristics at 500°C. This suggests that feedstock-related differences between RA 500 and DF 500 were not strongly expressed in the Raman I_D/I_G ratios. The I_D/I_G ratios of DF 350, DF 500, and DF 700 were 0.66, 0.68, and 0.80, respectively. Within the temperature range examined, the increase in the I_D/I_G ratio indicates changes in the relative contributions of the D and G bands as the carbon structure underwent thermal reorganization. A similar increase at higher pyrolysis temperatures was reported by Chatterjee et al. (2020) for biochar produced from miscanthus (0.65–0.88), switchgrass (0.70–0.88), corn stover (0.58–0.83), and sugarcane bagasse (0.59–1.01) at 500°C–800°C.

The observed trend may partly reflect structural changes associated with volatile and gas evolution during pyrolysis. This process can contribute to structural rearrangement within the carbon matrix. This same trend was also reported in a study carried out by Barszcz et al. (2024). Their study reported that biochar structure became disordered as the pyrolysis temperature increased, despite exhibiting better thermal properties. The increase in I_D/I_G observed between 350°C and 700°C should therefore be interpreted as changes in carbon structure during thermal reorganization rather than evidence for or against extensive graphitization. The temperatures examined in this study are relatively low for extensive graphitic ordering of biomass-derived carbon.

In addition to Raman spectroscopy, FT-IR was used to evaluate biochar surface functional groups. Figure 3 shows the FT-IR spectra, with Figure 3a comparing DF 500 and RA 500. The main spectral difference occurred near ~1400 cm^{-1}, which corresponds to C-H deformation in cellulose and hemicellulose (Woźniak et al. 2022) and was more pronounced in RA 500. This suggests that RA retained more aliphatic C-H bonds than DF after pyrolysis at 500°C. This region may also overlap with

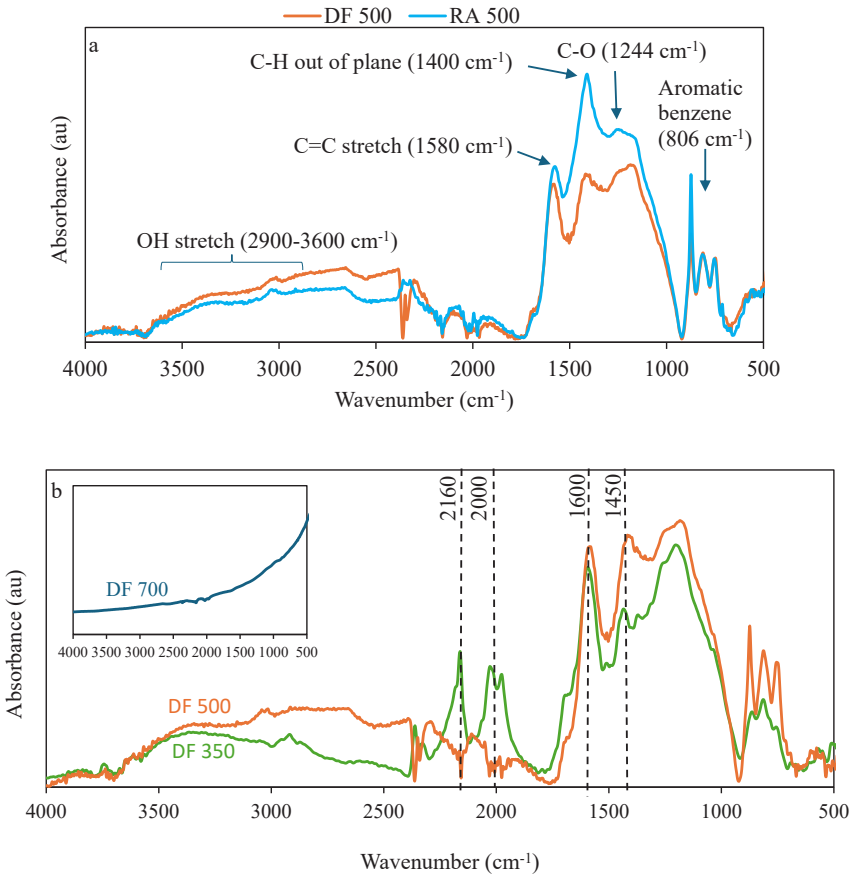


Figure 3. FT-IR spectra comparing the functional group peaks on (a) the effects of biomass feedstock on DF 500 and RA 500; and (b) the temperature effects on DF 350, DF 500, and DF 700.

aliphatic C-H from lignin retained after pyrolysis. The stronger RA 500 band may reflect the hardwood lignin composition of RA, which contains syringyl lignin in addition to guaiacyl lignin. Syringyl lignin is less cross-linked than guaiacyl lignin, which is dominant in softwoods such as DF (Stewart 2008). These differences in lignin structure may influence carbon condensation and functional-group retention during pyrolysis and may therefore contribute to the contrasting FT-IR features of RA 500 and DF 500. The role of feedstock composition in these differences is discussed further in the Effect of chemical composition section. Jackson et al. (2013) similarly reported that pine softwood biochar was more oxidation-resistant at higher temperatures than hardwood oak biochar because of its higher lignin content. DF 500 and RA 500 also showed similar peaks between 1000 and 1250 cm^{-1}, indicating C-H in-plane bending (Li et al. 2023), with the peak near 1100 cm^{-1} attributed to aromatic ester C-O bonds (Vaughn et al. 2013). Considering the MC results in Table 1 and the FT-IR findings, the lower MC of RA 500 is likely more strongly related to pore structure than surface chemistry.

Narrow bands with strong signals were observed near 1600 cm^{-1}, corresponding to aromatic C=C stretching. Weaker bands at 750–900 cm^{-1} are attributed to aromatic structures. Broad absorption at 3200–3400 cm^{-1}, attributed to O-H stretching, indicated hydroxyl groups from residual cellulose, hemicellulose, or absorbed water (Leng et al. 2021). This band was slightly stronger in DF than RA, although the difference was less pronounced than for the C-H band discussed above. Weak peaks at 2800–3000 cm^{-1} corresponded to aliphatic C-H stretching (Lu et al. 2005), while peaks near 2000–2200 cm^{-1} were likely due to aromatic combination bands or overtones, or C≡C functionalities (Kumar 2006).

Among the three pyrolysis temperatures shown in Figure 3b, DF 700 showed no significant peaks, suggesting minimal detectable surface functional groups and less polar surface chemistry. In contrast, DF 350 and DF 500 displayed distinct peaks, with DF 350 showing stronger absorbance. The more pronounced O-H stretching in DF 350 suggests greater retention of hydroxyl-containing structures from residual cellulose, hemicellulose, or adsorbed water. Stronger C-H in-plane bending and C-O bands further indicate higher oxygen-containing functional group abundance, consistent with increased deoxygenation at higher pyrolysis temperatures. For DF 700, dehydration, deoxygenation, and aromatization likely contributed to the substantial reduction in detectable functional groups signals (Liu et al. 2018). Elemental analysis was therefore conducted to help interpret the FT-IR results.

Elemental analysis

Elemental analysis (EA) provides information on the chemical composition of biomass and biochar, including changes in carbon, hydrogen, and oxygen contents with pyrolysis temperature and treatment. These results complement the spectroscopy analyses by indicating the degree of carbonization and changes in elemental composition as a function of pyrolysis conditions. Table 3 presents the elemental composition of DF biomass; DF biochar produced at 350°C, 500°C, and 700°C; RA biomass; and RA biochar produced at 500°C. Carbon content increased from 48% in raw DF biomass to 75% after pyrolysis at 350°C, then increased further to 81% at 500°C and 87% at 700°C. Similarly, carbon content in RA increased from 48% in raw biomass to 71% after pyrolysis at 500°C.

RA 500 had lower relative carbon content than all DF biochar, consistent with the FT-IR results showing greater retention of aliphatic C-H in RA 500 and greater aromatization in DF 500. Oxygen content showed the opposite trend, decreasing with increasing pyrolysis temperature. RA 500 had the highest post-pyrolysis oxygen content (25%), suggesting greater retention of oxygen-containing structures, consistent with the FT-IR evidence for hydroxyl-containing groups. Fuertes et al. (2010) reported a similar finding for corn stover hydrochar, which retained stable functional groups and had an O/C atomic ratio of 0.27. Oxygen-to-carbon (O/C) and hydrogen-to-carbon (H/C) ratios are commonly used to assess biochar chemical stability and polarity. The Van Krevelen diagram in Figure 4

Table 3. Relative elemental composition of DF and RA biomass and biochar.

	Relative composition (%)				Ratio	
Sample	C	H	N	O	O/C	H/C
DF biomass	47.81	6.42	0.34	45.43	0.71	1.60
RA biomass	48.40	6.21	0.31	45.08	0.70	1.53
RA 500	70.84	3.18	1.24	24.74	0.26	0.54
DF 350	74.63	4.24	0.44	20.70	0.21	0.68
DF 500	80.65	2.96	0.76	15.63	0.15	0.44
DF 700	87.34	1.61	0.60	10.46	0.09	0.22

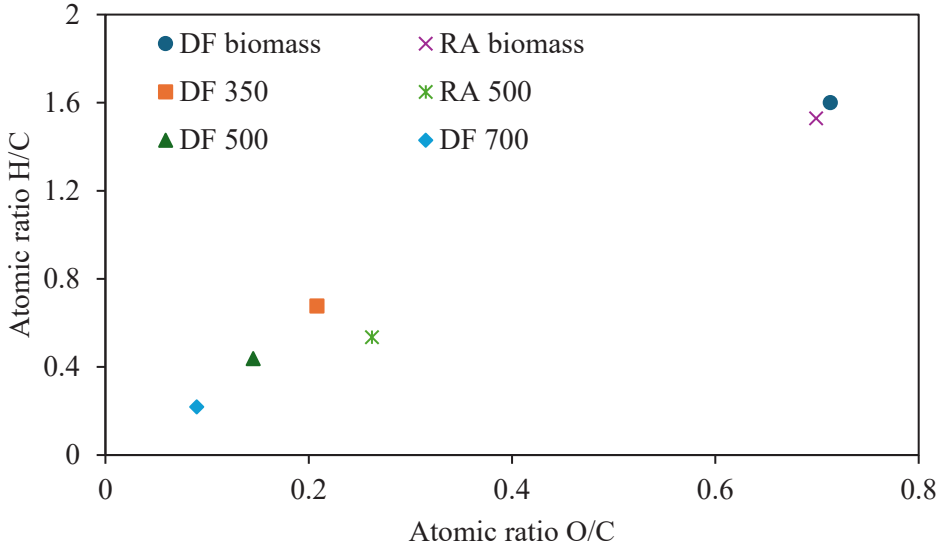


Figure 4. Plot of atomic ratio H/C vs. O/C of the biomass and biochar samples.

plots atomic H/C against O/C ratios for all samples. DF and RA biomass had the highest H/C and O/C ratios, characteristic of raw lignocellulosic biomass (Zhang et al. 2024). With increasing pyrolysis temperature, both ratios decreased, reflecting progressive dehydration and decarboxylation, hydrogen and oxygen loss, carbon enrichment, and increased aromaticity (Wang et al. 2022).

These results indicate that low-temperature biochar retained more oxygenated groups, consistent with FT-IR results, and may therefore offer more reactive sites for subsequent chemical modification. Additionally, this means that the polarity of the biochar was reduced with increasing pyrolysis temperature (Novak et al. 2009; Sun et al. 2012).

Referring to the Raman and FT-IR results, the comparable I_D/I_G ratios of RA 500 and DF 500 indicate that the differences observed in functional group retention and elemental composition were not accompanied by a large difference in the Raman I_D/I_G ratio at 500°C.

Thermogravimetric analysis

TGA provided insight into the thermal decomposition behavior and stability of the raw biomass and biochar samples by monitoring weight loss as a function of temperature. The TGA results provide complementary information on thermal stability that can be compared with the FT-IR and elemental analysis results. As shown in Figure 5a, the thermograms of DF and RA biomass resembled those of typical lignocellulosic materials. The initial stage, from room temperature to ~100°C, corresponded to moisture evaporation, followed by steep degradation associated with thermal decomposition of cellulose and hemicellulose (Yang et al. 2007). Table 4 summarizes the onset temperatures and residue percentages of the samples.

The onset of steep degradation differed between DF and RA biomass, occurring at 263°C for DF and 305°C for RA, followed by gradual lignin degradation over a broader temperature range. The lower onset temperature of DF indicates earlier thermal decomposition of its lignocellulosic components. For the biochar, DF 500 had a higher degradation onset temperature than RA 500 (529°C vs. 502°C), indicating greater resistance to thermal degradation. This is consistent with the lower H/C and O/C ratios and weaker aliphatic and oxygen-containing FT-IR features observed for DF 500. In addition, DF biochar had lower residual mass than RA biochar.

TGA of biochar produced at 350°C, 500°C, and 700°C showed that thermal stability increased with pyrolysis temperature. DF 700 exhibited the lowest weight loss, indicating a carbon-rich

Table 4. TGA onset temperature and residue of the biomass and biochar samples.

Sample	Onset temperature (°C)	Residue (%)
DF biomass	263	81
RA biomass	305	89
RA 500	502	35
DF 350	363	47
DF 500	529	22
DF 700	546	10

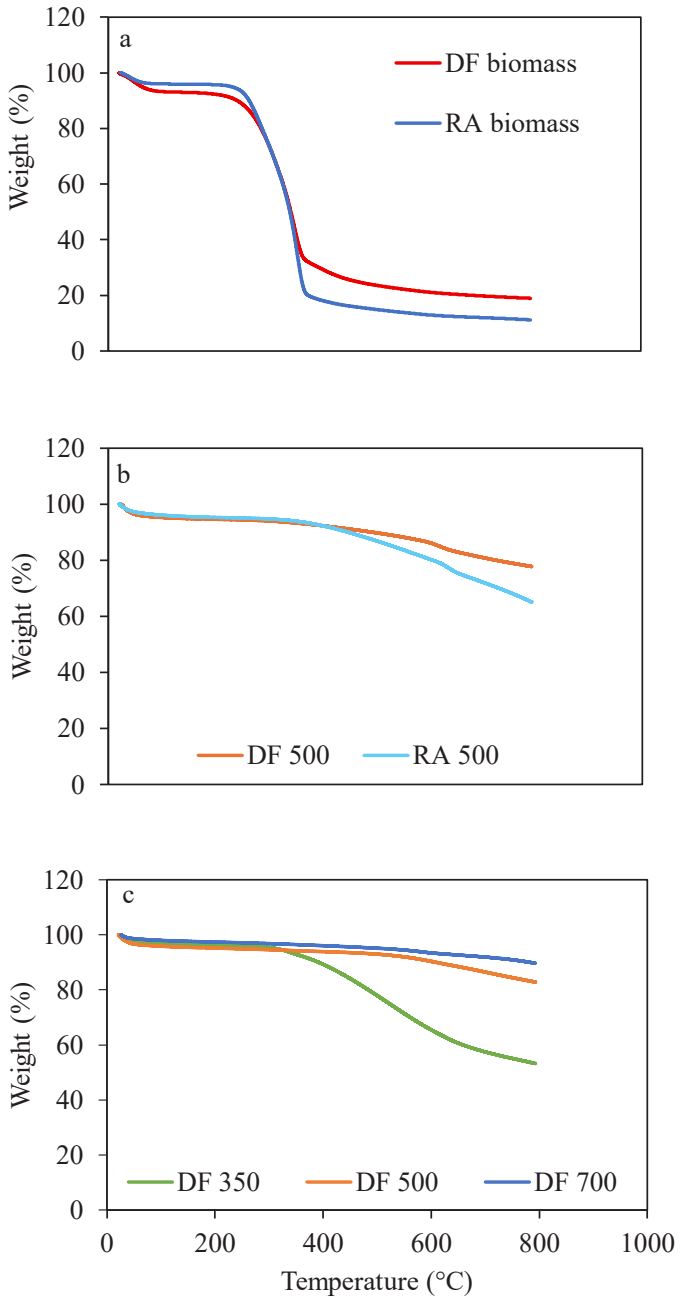


Figure 5. TGA profiles comparing (a) DF and RA biomass; (b) DF and RA biochar produced at 500°C; and (c) DF biochar produced at three different temperatures (350°C, 500°C, and 700°C).

structure, consistent with the low O/C and H/C ratios from elemental analysis (Table 3) and the FT-IR results (Figure 3b). In contrast, DF 350 showed lower thermal stability due to retained functional groups, with degradation onset at 363°C associated with cellulose and hemicellulose decomposition. This result also agrees with the elemental and FT-IR analyses. Residual mass at 800°C decreased substantially with pyrolysis temperature, from 47% for DF 350 to 10% for DF 700. This trend is consistent with previous studies showing that higher pyrolysis temperatures produce biochar with greater carbon content and thermal resilience (Keiluweit et al. 2010; Ahmad et al. 2012).

Effect of chemical composition

RA used in this study contained 34.4 ± 5.3% cellulose, 23.5 ± 4.5% hemicellulose, and 32.3 ± 2.3% lignin, whereas DF contained 35.8 ± 2.4% cellulose, 19.2 ± 7.8% hemicellulose, and 36.8 ± 0.9% lignin (Macias et al. 2026). Cellulose content was similar between the two feedstocks, suggesting that the contrasting behavior at 500°C is more likely associated with differences in hemicellulose content, lignin chemistry, ash, and extractives than with differences in initial cellulose content. The higher hemicellulose content of RA, together with its syringyl-guaiacyl lignin composition, may provide a larger initial pool of oxygen- and hydrogen-rich precursors during pyrolysis. Hemicellulose, the most thermally labile structural biopolymer, degrades at approximately 220°C–315°C and can contribute residual aliphatic C-H fragments to the char matrix at 500°C. Syringyl lignin, which contains two methoxy groups per aromatic ring and is linked mainly by labile β-O-4 ether bonds, can also release aliphatic and oxygenated fragments during cleavage rather than fully condensing into an aromatic structure. Consistent with these compositional differences, RA 500 showed less extensive deoxygenation and aromatization at 500°C, retaining pronounced C-H (~1400 cm^{-1}) and O-H (3200-3600 cm^{-1}) FT-IR bands, as well as elevated O/C (0.26) and H/C (0.54) ratios.

In contrast, the higher guaiacyl lignin content of DF may contribute to carbon condensation. Guaiacyl units contain one methoxy group and are connected by more thermally resistant 5-5 and β-5 carbon-carbon bonds, which resist cleavage and favor aromatic ring fusion as temperature increases. At 500°C, this structure promotes elimination of aliphatic and oxygenated functional groups, producing DF 500 with lower O/C (0.15) and H/C (0.44) ratios and lower TGA residue than RA 500 (22% vs. 35%). These results suggest a more aromatized, oxygen-depleted carbon skeleton in DF 500.

Differences in ash and extractives may have further contributed to the feedstock-dependent behavior. RA had a higher ash content than DF (1.260 ± 0.001% vs. 0.750 ± 0.001%) (Macias et al. 2026), indicating a greater initial mineral fraction that could contribute to the higher residue observed for RA 500 during TGA. Minerals may also influence pyrolysis reactions by catalyzing dehydration, decarboxylation, and char-forming reactions, which could partially affect the retention of oxygenated structures and the final carbon matrix. In contrast,

DF contained substantially higher extractives than RA (8.8 ± 1.3% vs. 3.5 ± 1.0%). These extractives may volatilize or thermally degrade during pyrolysis, contributing to volatile release. Therefore, hemicellulose content and lignin chemistry provide plausible explanations for the contrasting behavior of RA 500 and DF 500, while differences in ash and extractives may act as additional modifiers of thermal degradation, residue formation, and carbon condensation.

It is worth noting that a limitation of the present study is that red alder biochar was produced only at 500°C, whereas Douglas-fir biochar was evaluated across 350°C, 500°C, and 700°C. Consequently, temperature-dependent trends can be assessed only for Douglas-fir, while feedstock-related differences are limited to the direct comparison between Douglas-fir and red alder at 500°C. The current design therefore does not allow feedstock vs temperature interactions to be independently evaluated. Future work should evaluate both feedstocks across a common temperature range to more clearly separate feedstock effects from temperature-dependent responses.

Temperature-dependent structural evolution

The SEM micrographs were obtained from DF and RA biochar produced in a separate slow pyrolysis experiment and were not

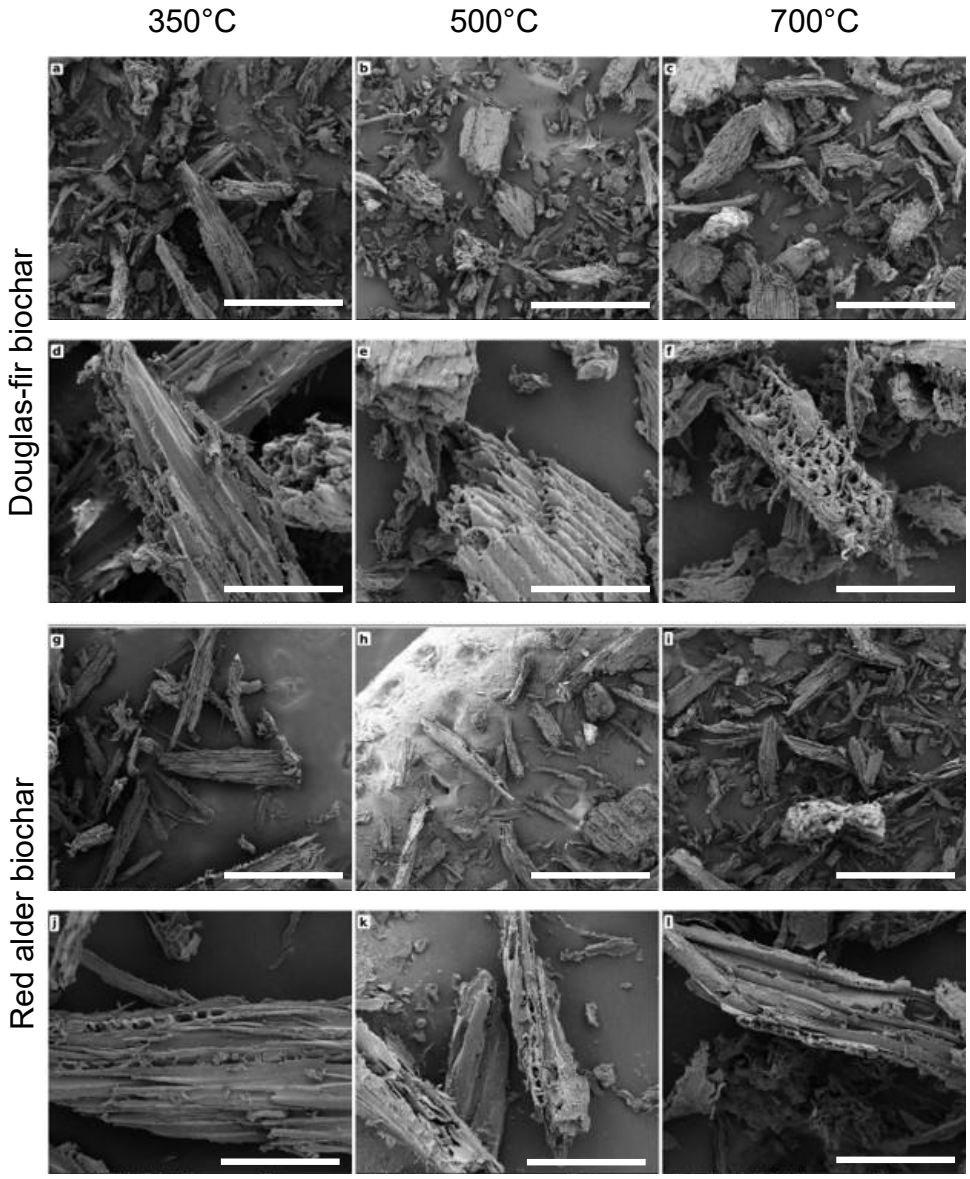


Figure 6. Scanning electron microscopy (SEM) images of biochar samples pyrolyzed at 350°C, 500°C, and 700°C. The top two rows correspond to DF biochar, while the bottom two rows correspond to RA biochar. For each wood species, the first row shows images acquired at 100× magnification (scale bar = 500 μm), and the second row shows higher magnification images at 500× (scale bar = 100 μm).

collected from the fast-pyrolysis biochar characterized earlier. These SEM images are included as complementary qualitative observations of temperature-dependent morphological changes and are not interpreted as direct morphological evidence for the fast pyrolysis samples. Qualitative SEM observations showed changes in DF and RA surface morphology (Figure 6). At 350°C, both DF and RA biochar retained the fibrous, elongated architecture of their wood precursors and displayed open longitudinal channels consistent with preserved cell lumens (Figure 6d,j). At 500°C, both biochar showed greater structural disruption. DF exhibited regular transverse surface corrugation, consistent with cell wall shrinkage and partial collapse (Figure 6e), whereas RA showed heterogeneous conversion, with macroporosity developing in some fiber fragments (Figure 6k). At 700°C, both species exhibited more extensive cellular disruption. DF showed greater collapse of cell walls and elongated elements (Figure 6f), while RA developed elongated interlamellar pores formed by longitudinal cell-wall delamination (Figure 6l).

These observations are consistent with the sequential thermochemical decomposition of hemicellulose, cellulose, and lignin with increasing temperature, where residual lignin provides structural support at 350°C and near-complete biopolymer volatilization at 700°C yields a porous carbon skeleton.

Conclusions

This assessment of Douglas-fir and red alder biochar revealed clear differences in physicochemical properties, thermal behavior, and structural features related to feedstock composition and pyrolysis temperature. A key finding, supported by FT-IR, elemental analysis, and TGA, was that RA 500 retained more hydrogenated and oxygenated structures than DF 500, as shown by stronger C-H and O-H bands and higher O/C and H/C ratios. These differences are consistent with the higher hemicellulose content and syringyl-guaiacyl lignin composition of RA, whereas the higher guaiacyl lignin content of DF may contribute to greater deoxygenation, aromatization, and carbon condensation. Across the Douglas-fir temperature series, biochar yield decreased with increasing temperature, whereas gas yield increased, particularly at 700°C. Proximate analyses showed that higher pyrolysis temperatures reduced volatile matter and increased fixed carbon, while pH shifted from moderately to strongly alkaline values. Raman analysis showed increasing I_D/I_G ratio with pyrolysis temperature, indicating changes in carbon structure during thermal reorganization. Feedstock differences were evaluated only at 500°C, while temperature effects were assessed only for Douglas-fir. Overall, the results show that differences in hemicellulose content, lignin chemistry, ash, and extractives may contribute to the contrasting properties of Douglas-fir and red alder biochar. These relationships provide a basis for further evaluation of woody biomass and pyrolysis conditions for biochar applications.

Data availability: Data will be made available upon request.

Competing interests: The authors declare no competing interests.

References

Ahmad M, Lee SS, Dou X, Mohan D, Sung J-K, Yang JE, Ok YS (2012) Effects of pyrolysis temperature on soybean stover- and peanut shell-derived biochar properties and TCE adsorption in water. Bioresour Technol 118:536–544. https://doi.org/10.1016/j.biortech.2012.05.042

Ahmad M, Rajapaksha AU, Lim JE, Zhang M, Bolan N, Mohan D, Vithanage M, Lee SS, Ok YS (2014) Biochar as a sorbent for contaminant management in soil and water: A review. Chemosphere 99:19–33 https://doi.org/10.1016/j.chemosphere.2013.10.071

Aldayyat EA, Saidan MN, Al-Hamamre Z, Al-Addous M, Alkasrawi M (2021) Pyrolysis of solid waste for bio-oil and char production in refugees' camp: A case study. Energies (Basel) 14 (13):3861. https://doi.org/10.3390/en14133861

ASTM International. (2021). ASTM D1762-84 Standard Test Method for Chemical Analysis of Wood Charcoal. American Society for Testing and Materials, West Conshohocken, PA, USA. https://doi.org/10.1520/D1762-84R21

Awad YM, Blagodatskaya E, Ok YS, Kuzyakov Y (2012) Effects of polyacrylamide, biopolymer, and biochar on decomposition of soil organic matter and plant residues as determined by 14C and enzyme activities. Eur J Soil Biol 48:1–10. https://doi.org/10.1016/j.ejsobi.2011.09.005

Barszcz W, Łożyńska M, Molenda J (2024) Impact of pyrolysis process conditions on the structure of biochar obtained from apple waste. Sci Rep 14:10501. https://doi.org/10.1038/s41598-024-61394-8

Bedia J, Peñas-Garzón M, Gómez-Avilés A, Rodriguez JJ, Belver C (2018) A Review on the Synthesis and Characterization of Biomass-Derived Carbons for Adsorption of Emerging Contaminants from Water. C (Basel) 4(4):63. https://doi.org/10.3390/c4040063

Bian R, Chen D, Liu X, Cui L, Pan G, Xie D, Zheng J, Zhang X, Zheng J, Chang A (2013) Biochar soil amendment as a solution to prevent Cd-tainted rice from China: Results from a cross-site field experiment. Ecol Eng 58:378–383. https://doi.org/10.1016/j.ecoleng.2013.07.031

Bolan N, Hoang SA, Beiyuan J, Gupta S, Hou D, Karakoti A, Joseph S, Jung S, Kim KH, Kirkham MB, Kua H, Kumar M, Kwon E, Ok YS, Perera V, Rinklebe J, Shaheen S, Sarkar B, Sarmah A, Van Zwieten L (2022) Multifunctional applications of biochar beyond carbon storage. International Materials Reviews 67(2):150–200 https://doi.org/10.1080/09506608.2021.1922047

Cárdenas-Aguiar E, Gascó G, Paz-Ferreiro J, Méndez A (2017) The effect of biochar and compost from urban organic waste on plant biomass and properties of an artificially copper polluted soil. Int Biodeterior Biodegradation 124:223–232. https://doi.org/10.1016/j.ibiod.2017.05.014

Chatterjee R, Sajjadi B, Chen WY, Mattern DL, Hammer N, Raman V, Dorris A (2020) Effect of Pyrolysis Temperature on PhysicoChemical Properties and Acoustic-Based Amination of Biochar for Efficient CO2 Adsorption. Front Energy Res 8. https://doi.org/10.3389/fenrg.2020.00085

Chaturvedi S, Singh SV, Dhyani VC, Govindaraju K, Vinu R, Mandal S (2023) Characterization, bioenergy value, and thermal stability of biochars derived from diverse agriculture and forestry lignocellulosic wastes. Biomass Convers Biorefin 13:879–892. https://doi.org/10.1007/s13399-020-01239-2

Chen B, Chen Z, Lv S (2011) A novel magnetic biochar efficiently sorbs organic pollutants and phosphate. Bioresour Technol 102(2):716–723. https://doi.org/10.1016/j.biortech.2010.08.067

Chhiti Y, Salvador S, Commandré JM, Broust F (2012) Thermal decomposition of bio-oil: Focus on the products yields under different pyrolysis conditions. Fuel 102:274–281. https://doi.org/10.1016/j.fuel.2012.06.098

Childres I, Jauregui LA, Park W, Cao H, Chen YP (2013) Raman spectroscopy of graphene and related materials. In: Jang, J.I., Ed., New Developments in Photon and Materials Research, NOVA Science Publishers, Inc., New York, 403–418. https://novapublishers.com/shop/new-developments-in-photon-and-materials-research/

Chisté L, Melo LCA, Jindo K, Silva CA (2024) Biochar-boron composites: synthesis, properties and agronomic effectiveness for eucalyptus seedlings. Chemical and Biological Technologies in Agriculture 11(154). https://doi.org/10.1186/s40538-024-00645-2

Das O, Sarmah AK, Bhattacharyya D (2015) A novel approach in organic waste utilization through biochar addition in wood/polypropylene composites. Waste Management 38:132–140. https://doi.org/10.1016/j.wasman.2015.01.015

Datsyuk V, Kalyva M, Papagelis K,Parthenios J, Tasis D, Siokou A, Kallitsis I, Galiotis C (2008) Chemical oxidation of multiwalled carbon nanotubes. Carbon N Y 46(6):833–840. https://doi.org/10.1016/j.carbon.2008.02.012

De Sousa DV, Guimarães LM, Félix JF, Ker JC, Schaefer CERG, Rodet MJ (2020) Dynamic of the structural alteration of biochar in ancient Anthrosol over a long timescale by Raman spectroscopy. PLoS One 15(3):e0229447. https://doi.org/10.1371/journal.pone.0229447

Demirbas A (2007) Effect of temperature on pyrolysis products from biomass. Energy Sources, Part A: Recovery, Utilization and Environmental Effects 29(4):329–336. https://doi.org/10.1080/009083190965794

Domingues RR, Trugilho PF, Silva CA, Melo ICNAd, Melo LCA, Magriotis ZM, Sánchez-Monedero MA (2017) Properties of biochar derived from wood and high-nutrient biomasses with the aim of agronomic and environmental benefits. PLoS One 12(5):e0176884. https://doi.org/10.1371/journal.pone.0176884

Dubinin MM, Radushkevich LV (1947) Equation of the characteristic curve of activated charcoal. Proceedings of the Academy of Sciences of the USSR: Physical Chemistry Section 55:331-337.

Dubinin MM, Zaverina ED, Radushkevich, L. V. (1947). Sorption and structure of active carbons. I. Adsorption of organic vapors. Zhurnal Fizicheskoi Khimii 21(3), 151–162.

Fuertes AB, Arbestain MC, Sevilla M, Maciá-Agulló JA, Fiol S, López R, Smernik RJ, Aitkenhead WP, Arce F, Macias F (2010) Chemical and structural properties of carbonaceous products obtained by pyrolysis and hydrothermal carbonisation of corn stover. Australian Journal of Soil Research 48(7):618–626. https://doi.org/10.1071/SR10010

Gaskin JW, Steiner C, Harris K, Das KC, Bibens B (2008) Effect of low-temperature pyrolysis conditions on biochar for agricultural use. Trans ASABE 51(6): 2061–2069. https://doi.org/10.13031/2013.25409

Glaser B, Lehmann J, Zech W (2002) Ameliorating physical and chemical properties of highly weathered soils in the tropics with charcoal - A review. Biol. Fertil. Soils 35:219–230. https://doi.org/10.1007/s00374-002-0466-4

Gupta S, Kua HW, Koh HJ (2018) Application of biochar from food and wood waste as green admixture for cement mortar. Science of the Total Environment 619–620:419–435. https://doi.org/10.1016/j.scitotenv.2017.11.044

Hassan M, Liu Y, Naidu R, Parikh SJ, Du J, Qi F, Willett IR (2020) Influences of feedstock sources and pyrolysis temperature on the properties of biochar and functionality as adsorbents: A meta-analysis. Science of the Total Environment 744:140714. https://doi.org/10.1016/j.scitotenv.2020.140714

He M, Hu Z, Xiao B, Li J, Guo X, Luo S, Yang F, Feng Y, Yang G, Liu S (2009) Hydrogen-rich gas from catalytic steam gasification of municipal solid waste (MSW): Influence of catalyst and temperature on yield and product composition. Int J Hydrogen Energy 34(1):195–203. https://doi.org/10.1016/j.ijhydene.2008.09.070

Ippolito JA, Cui L, Kammann C, Wrage-Mönnig N, Estavillo JM, Fuertes-Mendizabal T, Cayuela ML, Sigua G, Novak J, Spokas K, Borchard N (2020) Feedstock choice, pyrolysis temperature and type influence biochar characteristics: a comprehensive meta-data analysis review. Biochar 2:421–438. https://doi.org/10.1007/s42773-020-00067-x

Jackson MA, Eberhardt TL, Boateng AA, Mullen CA, Groom LH (2013) Evaluation of biochars by temperature programmed oxidation/mass spectrometry. Bioresources 8(4):5461–5474. https://doi.org/10.15376/biores.8.4.5461-5474

Kamarudin NS, Dahalan FA, Hasan M, An OS, Parmin NA, Ibrahim N, Hamdzah M, Zain NAM, Muda K, Wikurendra EA (2022) Biochar: A review of its history, characteristics, factors that influence its yield, methods of production, application in wastewater treatment and recent development. Biointerface Res Appl Chem 12(6):7914–7926. https://doi.org/10.33263/BRIAC126.79147926

Kan T, Strezov V, Evans TJ (2016) Lignocellulosic biomass pyrolysis: A review of product properties and effects of pyrolysis parameters. Renewable and Sustainable Energy Reviews 57:1126–1140. https://doi.org/10.1016/j.rser.2015.12.185

Keiluweit M, Nico PS, Johnson M, Kleber M (2010) Dynamic molecular structure of plant biomass-derived black carbon (biochar). Environ Sci Technol 44(4):1247–1253. https://doi.org/10.1021/es9031419

Keshvardoostchokami M, Braghiroli FL, Neculita CM, Koubaa A (2023) Advances in modified wood-based adsorbents for contaminant removal: Valorization methods, modification mechanisms, and environmental applications. Current Forestry Reports 9:444–460. https://doi.org/10.1007/s40725-023-00200-6

Kumar S (2006) Spectroscopy of Organic Compounds. Dept of Chemistry 66: https://www.scribd.com/doc/146831979/Spectroscopy-of-Organic-Compounds

Kunii D, Levenspiel O (1997) Circulating fluidized-bed reactors. Chem Eng Sci 52(15):2471–2482. https://doi.org/10.1016/S0009-2509(97)00066-3

Legan M, Gotvajn AŽ, Zupan K (2022) Potential of biochar use in building materials. J. Environ. Manage. 309:114704. https://doi.org/10.1016/j.jenvman.2022.114704

Leng L, Xiong Q, Yang L, Li H, Zhou Y, Zhang W, Jiang S, Li H, Huang H (2021) An overview on engineering the surface area and porosity of biochar. Science of the Total Environment 763:144204. https://doi.org/10.1016/j.scitotenv.2020.144204

Li S, Galoustian T, Trejo H (2023) Biochar pyrolyzed with concentrated solar radiation for enhanced nitrate adsorption. J Anal Appl Pyrolysis 174:106131. https://doi.org/10.1016/j.jaap.2023.106131

Liu WJ, Jiang H, Yu HQ (2015) Development of Biochar-based functional materials: Toward a sustainable platform carbon material. Chem Rev 115:(22):12251–12285. https://doi.org/10.1021/acs.chemrev.5b00195

Liu Z, Niu W, Chu H, Zhou T, Niu Z (2018) Effect of the carbonization temperature on the properties of biochar produced from the pyrolysis of crop residues. Bioresources 13(2):3429–3446. https://doi.org/10.15376/biores.13.2.3429-3446

Lu R, Gan W, Wu BH, Zhang Z, Guo Y, Wang H-f (2005) C-H stretching vibrations of methyl, methylene and methine groups at the vapor/Alcohol (n = 1-8) interfaces. Journal of Physical Chemistry B 109(29):14118–14129. https://doi.org/10.1021/jp051565q

Macias, R. J., Ibrahim, A., Presley, G., Hafez, I., Simonsen, J., Alam, A. Sessions J, Susaeta A, Sierra-Jimenez V, Garcia-Perez, M. (2026). Transforming biomass forest residues into transport fuels part 1: Fast pyrolysis and catalytic hydrotreatment. Biomass and Bioenergy 215:109579. https://doi.org/10.1016/j.biombioe.2026.109579

Manyà JJ (2012) Pyrolysis for biochar purposes: A review to establish current knowledge gaps and research needs. Environ Sci Technol 46(15):7939–7954. https://doi.org/10.1021/es301029g

Manyà JJ, Azuara M, Manso JA (2018) Biochar production through slow pyrolysis of different biomass materials: Seeking the best operating

conditions. Biomass Bioenergy 117:115–123. https://doi.org/10.1016/j.biombioe.2018.07.019

Mohan D, Sarswat A, Ok YS, Pittman CU (2014) Organic and inorganic contaminants removal from water with biochar, a renewable, low cost and sustainable adsorbent - A critical review. Bioresour Technol 160:191–202. https://doi.org/10.1016/j.biortech.2014.01.120

Novak J, Lima I, Xing B, Gaskin JW, Steiner C, Das KC, Ahmedna M, Rehrah D, Watts DW, Busscher WJ, Schomberg H (2009) Characterization of designer biochar produced at different temperatures and their effects on a loamy sand. Annals of Environmental Science 3. https://openjournals.neu.edu/aes/journal/article/view/v3art5

Restuccia L, Ferro GA, Suarez-Riera D, Sirico A, Bernardi P, Belletti B, Malcevschi A (2020) Mechanical characterization of different biochar-based cement composites. Procedia Structural Integrity 25:226–233. https://doi.org/10.1016/j.prostr.2020.04.027

Shakoor MB, Ali S, Rizwan M, Bibi I, Riaz M, Khalil U, Niazi NK, Rinklebe J (2020) A review of biochar-based sorbents for separation of heavy metals from water. Int. J. Phytoremediation 22(2):111–126. https://doi.org/10.1080/15226514.2019.1647405

Sharma A, Pareek V, Zhang D (2015) Biomass pyrolysis - A review of modelling, process parameters and catalytic studies. Renewable and Sustainable Energy Reviews 50:1081–1096. https://doi.org/10.1016/j.rser.2015.04.193

Silber A, Levkovitch I, Graber ER (2010) PH-dependent mineral release and surface properties of cornstraw biochar: Agronomic implications. Environ Sci Technol 44(24):9318–9323. https://doi.org/10.1021/es101283d

Singh B, Dolk MM, Shen Q, Camps-Arbestain M (2017) Biochar : pH, electrical conductivity and liming potential. In: Singh B, Camps-Arbestain M, Lehmann J (eds), Biochar: A Guide to Analytical Methods, CSIRO Publishing, pp 23–38.

Sluiter A, Hames B, Ruiz R, Scarlata C, Sluiter J, Templeton D, Crocker D (2012) Determination of structural carbohydrates and lignin in biomass: Laboratory analytical procedure (LAP). National Renewable Energy Laboratory, Technical Report NREL/TP-510-42618; revised August 2012. https://docs.nlr.gov/docs/gen/fy13/42618.pdf

Sopeña F, Semple K, Sohi S, Bending G (2012) Assessing the chemical and biological accessibility of the herbicide isoproturon in soil amended with biochar. Chemosphere 88:77–83. https://doi.org/10.1016/j.chemosphere.2012.02.066

Stewart D (2008) Lignin as a base material for materials applications: Chemistry, application and economics. Ind Crops Prod 27(2):202–207. https://doi.org/10.1016/j.indcrop.2007.07.008

Suliman W, Harsh JB, Abu-Lail NI, Fortuna A-M, Dallmeyer I, Garcia-Perez M, (2016) Influence of feedstock source and pyrolysis temperature on biochar bulk and surface properties. Biomass Bioenergy 84:37–48. https://doi.org/10.1016/j.biombioe.2015.11.010

Sun J, He F, Pan Y, Zhang Z (2017) Effects of pyrolysis temperature and residence time on physicochemical properties of different biochar types. Acta Agric Scand B Soil Plant Sci 67(1):12–22. https://doi.org/10.1080/09064710.2016.1214745

Sun K, Gao B, Ro KS, Novak JM, Wang Z, Herbert S, Xing B (2012) Assessment of herbicide sorption by biochars and organic matter associated with soil and sediment. Environmental Pollution 163:167–173. https://doi.org/10.1016/j.envpol.2011.12.015

Sun Y, Gao B, Yao Y, Fang J, Zhang M, Zhou Y, Chen H, Yang L, (2014) Effects of feedstock type, production method, and pyrolysis temperature on biochar and hydrochar properties. Chemical Engineering Journal 240:574–578. https://doi.org/10.1016/j.cej.2013.10.081

Tagliaferro A, Rovere M, Padovano E, Bartoli M, Giorcelli M (2020) Introducing the novel mixed Gaussian-Lorentzian lineshape in the analysis of the Raman signal of biochar. Nanomaterials 10:1–19. https://doi.org/10.3390/nano10091748

Tang Q, Chen Y, Yang H, Liu M, Xiao H, Wu Z, Chen H, Naqvi SR (2020) Prediction of Bio-oil Yield and Hydrogen Contents Based on Machine Learning Method: Effect of Biomass Compositions and Pyrolysis Conditions. Energy and Fuels 34(9):11050–11060. https://doi.org/10.1021/acs.energyfuels.0c01893

Titiladunayo IF, McDonald AG, Fapetu OP (2012) Effect of temperature on biochar product yield from selected lignocellulosic biomass in a pyrolysis process. Waste Biomass Valorization 3:311–318. https://doi.org/10.1007/s12649-012-9118-6

Tomczyk A, Sokołowska Z, Boguta P (2020) Biochar physicochemical properties: pyrolysis temperature and feedstock kind effects. Rev Environ Sci Biotechnol 19:191–215. https://doi.org/10.1007/s11157-020-09523-3

Tripathi M, Sahu JN, Ganesan P (2016) Effect of process parameters on production of biochar from biomass waste through pyrolysis: A review. Renewable and Sustainable Energy Reviews 55:467–481. https://doi.org/10.1016/j.rser.2015.10.122

Vaughn SF, Kenar JA, Thompson AR, Peterson SC (2013) Comparison of biochars derived from wood pellets and pelletized wheat straw as replacements for peat in potting substrates. Ind Crops Prod 51:437–443. https://doi.org/10.1016/j.indcrop.2013.10.010

Wang Y, Gu X, Huang Y, Ding Z, Chen Y, Hu X (2022) Insight into biomass feedstock on formation of biochar-bound environmentally persistent free radicals under different pyrolysis temperatures. RSC Adv 12(30):19318–19326. https://doi.org/10.1039/d2ra03052g

Woźniak M, Gromadzka K, Kwaśniewska-Sip P, Cofta G, Ratajczak I (2022) Chitosan–caffeine formulation as an ecological preservative in wood protection. Wood Sci Technol 56:1851–1867. https://doi.org/10.1007/s00226-022-01426-6

Xu R-k, Zhao A-z, Yuan J-h, Jiang J (2012) pH buffering capacity of acid soils from tropical and subtropical regions of China as influenced by incorporation of crop straw biochars. J Soils Sediments 12:494–502. https://doi.org/10.1007/s11368-012-0483-3

Yaashikaa PR, Kumar PS, Varjani S, Saravanan A (2020) A critical review on the biochar production techniques, characterization, stability and applications for circular bioeconomy. Biotechnology Reports 28:e00570. https://doi.org/10.1016/j.btre.2020.e00570

Yang H, Yan R, Chen H, Lee DH, Zheng C (2007) Characteristics of hemicellulose, cellulose and lignin pyrolysis. Fuel 86:1781–1788. https://doi.org/10.1016/j.fuel.2006.12.013

Yuan JH, Xu RK, Zhang H (2011) The forms of alkalis in the biochar produced from crop residues at different temperatures. Bioresour Technol 102:. https://doi.org/10.1016/j.biortech.2010.11.018

Zhang S, Jia X, Wang X, Chen J, Cheng C, Jia X, Hu H (2024) Using the conditional process analysis model to characterize the evolution of carbon structure in *Taxodium ascendens* biochar with varied pyrolysis temperature and holding time. Plants 13(30):460. https://doi.org/10.3390/plants13030460

Zhang Y, He M, Wang L, Yan J, Ma B, Zhu X, Ok YS, Mechtcherine V, Tsang DCW (2022) Biochar as construction materials for achieving carbon neutrality. Biochar 4(59). https://doi.org/10.1007/s42773-022-00182-x

Zhao L, Cao X, Mašek O, Zimmerman A (2013) Heterogeneity of biochar properties as a function of feedstock sources and production temperatures. J Hazard Mater 256–257:1–9. https://doi.org/10.1016/j.jhazmat.2013.04.015